

Article

Topographical and Thermal Forcing in Favorable Circulation Pattern to Early Spring Precipitation over the Southeastern Tibetan Plateau

Yaoxian Yang^{1,2,*}, Zeyong Hu^{1,2,*}, Maoshan Li³, Haipeng Yu^{1,2}, Weiqiang Ma^{4,5,6}  and Weiwei Fan^{1,2,7}

- ¹ Key Laboratory of Land Surface Process and Climate Change in Cold and Arid Regions, Northwest Institute of Eco-Environment and Resources, Chinese Academy of Sciences, Lanzhou 730000, China; yangyaoxian@nieer.ac.cn (Y.Y.); yuhp@lzb.ac.cn (H.Y.); fanweiwei19@mails.ucas.ac.cn (W.F.)
 - ² Nagqu Station of Plateau Climate and Environment, Northwest Institute of Eco-Environment and Resources, Chinese Academy of Sciences, Nagqu 852000, China
 - ³ Plateau Atmosphere and Environment Key Laboratory of Sichuan Province, College of Atmospheric Science, Chengdu University of Information Technology, Chengdu 610225, China; lims@cuit.edu.cn
 - ⁴ Land-Atmosphere Interaction and Its Climatic Effects Group, State Key Laboratory of Tibetan Plateau Earth System, Resources and Environment (TPESRE), Institute of Tibetan Plateau Research, Chinese Academy of Sciences, Beijing 100101, China; wqma@itpcas.ac.cn
 - ⁵ National Observation and Research Station for Qomolangma Special Atmospheric Processes and Environmental Changes, Dingri 858200, China
 - ⁶ College of Atmospheric Science, Lanzhou University, Lanzhou 730000, China
 - ⁷ College of Earth and Planetary Sciences, University of Chinese Academy of Sciences, Beijing 100049, China
- * Correspondence: zyhu@lzb.ac.cn



Citation: Yang, Y.; Hu, Z.; Li, M.; Yu, H.; Ma, W.; Fan, W. Topographical and Thermal Forcing in Favorable Circulation Pattern to Early Spring Precipitation over the Southeastern Tibetan Plateau. *Atmosphere* **2022**, *13*, 973. <https://doi.org/10.3390/atmos13060973>

Academic Editor: Eduardo García-Ortega

Received: 28 April 2022

Accepted: 6 June 2022

Published: 15 June 2022

Publisher's Note: MDPI stays neutral with regard to jurisdictional claims in published maps and institutional affiliations.



Copyright: © 2022 by the authors. Licensee MDPI, Basel, Switzerland. This article is an open access article distributed under the terms and conditions of the Creative Commons Attribution (CC BY) license (<https://creativecommons.org/licenses/by/4.0/>).

Abstract: During the boreal spring (March–May), the precipitation that occurs from March over the southeastern Tibetan Plateau (TP) can account for 20–40% of the total annual amount. The origin of this phenomenon has not been clearly understood from a climatological perspective. In this study, the role of topographical and thermal forcing on the precipitation over the southeastern TP in early spring (March) was investigated through sensitivity numerical simulations based on general circulation model. The simulated results show the favorable circulation and static stability to early spring precipitation over the southeastern TP when the model is simultaneously forced by realistic topography, zonal symmetric radiative equilibrium temperature, and diabatic heating over the TP and its surrounding areas. The quasi-stationary wave pattern over the Eurasian continent forced by realistic and TP topographical forcing leads to prolonged low pressure and intensified zonal winds over the southeastern TP due to quasi-steady wave activities. Thermal forcing experiments reveals that sensible heating over the southeastern TP not only strengthens the cyclonic circulation, ascending motion and statically unstable over the southeastern TP through thermal adaptation and the Sverdrup balance, but also triggers an anticyclone at upper tropospheric level extending from north of the Bay of Bengal to the eastern TP, which further favors precipitation over the southeastern TP. This work will provide useful background information for spring climate prediction over the TP.

Keywords: topographic and thermal forcing; Tibetan Plateau; atmospheric circulation; early spring; precipitation

1. Introduction

The Tibetan Plateau (TP) precipitation and its variation not only are the key processes in sustainable recharge of the “Asian water tower” and for prevention of natural disasters [1–3], but also modulate the characteristics of the TP heat source, which can further change the atmospheric circulation over the TP and its surrounding areas [4–6]. The seasonal evolution of TP precipitation is mainly affected by the meridional shift of westerlies over the Eurasian Continent and the onset of Asian Summer Monsoonal flow [5,7]. In

climatology, during the boreal winter, dynamical branching of mid-latitude westerlies by TP causes heavy precipitation over the western TP in the form of snowfall [3,8]. While, with the onset of monsoonal flow from the Bay of Bengal (BOB) to the TP, abundant moisture transport from the Indian Ocean and BOB converges in the southern TP and generates high levels of precipitation [5,9].

As the transitional period from winter to summer general circulation, springtime precipitation over the TP has its own unique features and effects. Based on ground-based observations and satellite data, a previous study provided evidence that the contribution of pre-monsoon (March–May) precipitation from high altitudes of the Central Himalayas to the southeastern TP to annual precipitation exceeds 30%. This unique spatial pattern may be associated with warm advection and water vapor transport through southwesterly winds from the Bay of Bengal [10]. From a weather perspective, snowstorms predominantly occur in the spring over the TP, causing serious economic losses [3]. Meanwhile, the springtime snow anomaly over the TP changes the thermal condition and heat source, thereby exerting an influence on the onset of the Asian Summer Monsoon and summer precipitation over its downstream regions [11,12]. Therefore, further study on the mechanisms responsible for this unique phenomenon, especially on the topographical and climatology mean thermal forcing over the TP in early spring circulation, can more deeply understand the formation of background circulation, which is important for improving the predictability of precipitation over the TP and its downstream regions, and for reducing the economic losses from snow-related disasters over the TP. However, less attention has been paid to this field, especially on the generation of favorable atmospheric circulation patterns of the spatial distribution of springtime precipitation over the TP from a climatological perspective.

As the highest plateau in the world, the TP is characterized as a heterogeneous surface and uplifted heat source [5,13]. The TP's mechanical and thermal impacts on the atmospheric circulation and formation of the climate of the Northern Hemisphere have been studied using theoretical diagnosis and numerical simulations since the mid twentieth century. In 1950, Both Yeh and Bolin [14,15] proved that giant highlands can split the background westerlies, to converge in the downstream regions, and this conclusion can explain the formation of the wintertime Eastern Asian Jet. Due to the heterogeneity of topographic slope and orientation, Rossby wave propagation over the southern flank of the TP is obviously faster than that over the northern flank of the TP [16]. Moreover, the asymmetric dipole atmospheric circulation pattern triggered by the mechanical forcing of the TP can form a warm center over central Asia, an arid climate over India, a humid climate over the Indio-China peninsula, and persistent precipitation over South China, through the associated temperature and moisture advection [4]. Previous studies indicated that in climatology, mean springtime sensible heating is the dominant component of the TP heat source, and may be an important factor in the seasonal evolution of atmospheric circulation over the Eurasian continent, as it can generate cyclonic circulation over the lower troposphere, trigger Rossby wave propagation, and promote the reversion of land–sea thermal contrast, to affect the persistent precipitation over South China and even the summer monsoon onset [5,17,18].

Despite the great efforts have putted into researching the climate effects of topographical and thermal forcing over the TP [5,14,15,18,19], however, less attention has been paid to their impacts on atmospheric circulation at monthly mean timescale in springtime. Additionally, the mechanism of the formation of pre-monsoon precipitation on the southeastern TP has not been explained clearly from a climatological perspective. For example, what is the favorable atmospheric circulation for early spring precipitation over the southeastern TP? How does the topographical and thermal aspects of the TP affect the generation of this pattern, respectively?

This paper mainly focuses on the climatological mean precipitation and atmospheric circulation in March, when the precipitation occurs on the southeastern TP, and aims to answer the abovementioned questions by investigating the climatological mean circulation and utilizing a set of numerical sensitivity tests. The rest of this study is organized as

follows: In Section 2, the general circulation model (GCM), data, and methods of analysis used in this study are described. Section 3 investigates the topographical and thermal impacts of the TP on the atmospheric circulation, based on a set of sensitivity experiments. A summary of the main findings and discussion of the potential for future research is presented in Section 4.

2. Model Experiments, Data, and Methods

2.1. Model Experiments and Data

The dry spectral dynamical core of the NCAR(National Center for Atmospheric Research, Boulder, The United States of America) Community Atmosphere Model version 5.4, with an idealized physical configuration based on Held and Suarez's parameterization [20] and a horizontal resolution within a spectral T85 truncation were used in the numerical experiments. The radiative forcing was parameterized as Newtonian relaxation to a zonal symmetric equilibrium temperature, and external diabatic heating could be imposed in the thermal equation. Additionally, the parameterized surface radiative equilibrium temperature and atmospheric optical thickness were considered using the methods of Schneider and Boradoni, Siu and Bowman [21,22] and Schneider [23], respectively. The momentum damping was confined in $\eta \geq 0.85$ in the hybrid vertical level [22]. The thermal damping strength in the free atmosphere and surface was prescribed as $1/40 \text{ day}^{-1}$ and $1/4 \text{ day}^{-1}$, respectively. Since the scientific question in the present study is the steady atmospheric responses to topographic and Tibetan Plateau thermal forcing in early spring, 5 years of perpetual integration with maximum surface radiative equilibrium temperature at the equator were used, which were set as 315 K and reduced by 60 K to poles in each experiment, and the last 3 years were used in a further study. The original topographic data used in the dry spectral dynamical core were from the United States Geological Survey dataset. In total, four experiments were carried out, including a control run without topographic forcing and external thermal heating (Notopo), three sensitivity experiments (Table 1) with realistic topographic forcing over the region of $70.3^\circ \text{ E} \sim 120.9^\circ \text{ E}$, $21.7^\circ \text{ N} \sim 60.9^\circ \text{ N}$ (TP_topo) (Figure 1), and realistic topographic forcing all over the world (Topo) and realistic topographic forcing all over the world with sensible heating over the southeastern TP and its surrounding areas (TP_sh).

Table 1. Configuration of topographical and thermal forcing in the numerical experiments.

Experiment Name	Experiment Configuration
Notopo	Without terrain and radiative forcing.
TP_topo	With realistic terrain over $70.3^\circ \text{ E} \sim 120.9^\circ \text{ E}$, $21.7^\circ \text{ N} \sim 60.9^\circ \text{ N}$ and radiative forcing.
Topo	With realistic terrain radiative forcing.
TP_sh	With realistic terrain, radiative forcing, and vertical diffusion heating over the Tibetan Plateau and its surrounding areas.

To carry out the thermal forcing experiment, the vertical diffusion heating, which mainly reflects surface sensible heating within a horizontal resolution of $0.5625^\circ \times 0.5625^\circ$ at hybrid levels, from the Japanese 55-year reanalysis (JRA-55) dataset [24] was used in the TP_sh test. Following Sardeshmukh and Hoskins's method [25], the spatially smoothed climatological mean zonal deviation of the vertical diffusion heating could be obtained, then we confined it over the region ($84.4^\circ \text{ E} \sim 120.9^\circ \text{ E}$, $-0.7^\circ \text{ N} \sim 40^\circ \text{ N}$) and considered the surface sensible heating in the TP_sh test. The column integrated heat source (Figure 2a) and the area mean (within the domain of $(24.5^\circ \text{ N} \sim 30.1^\circ \text{ N}$, $95.6^\circ \text{ E} \sim 101.25^\circ \text{ E})$ vertical profile (Figure 2b)) are displayed in Figure 2. To verify the simulated results, ERA5 reanalysis data [26] on pressure level and precipitation data derived from the China Meteorological Administration were used in present study. The abovementioned data covers from 1980 to 2017.

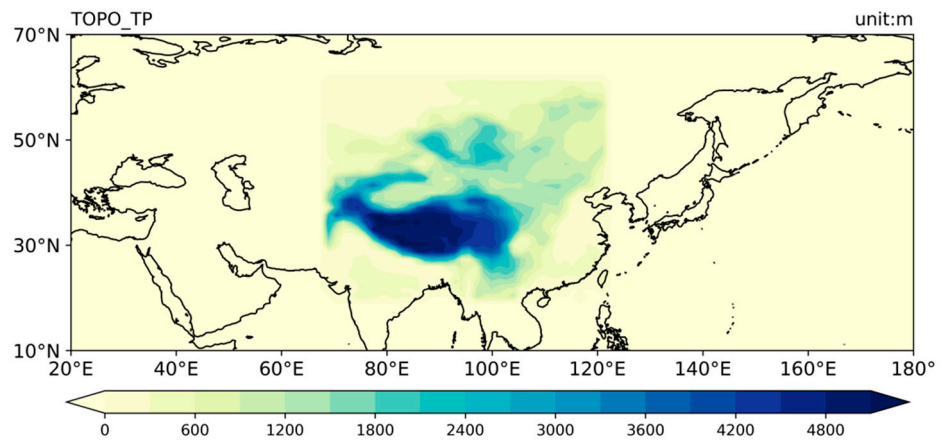


Figure 1. Topographical configuration (unit: m) for the experiment with the Tibetan Plateau and its surrounding areas.

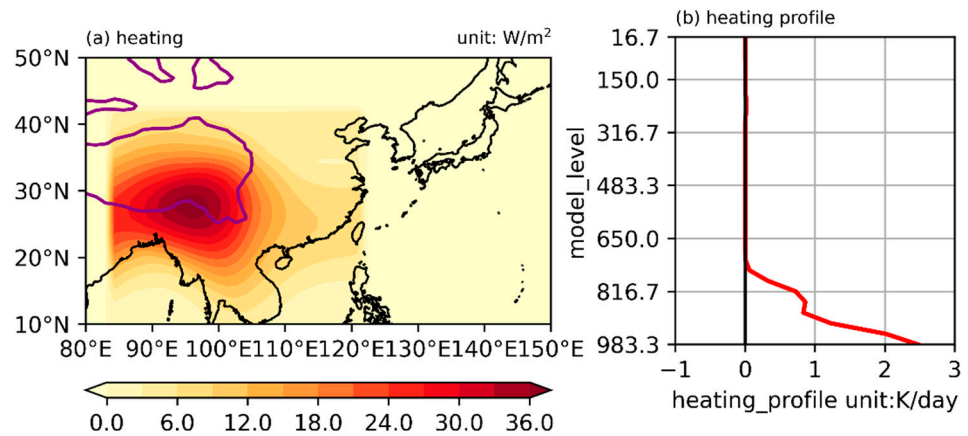


Figure 2. (a) The imposed sensible heating (unit: W/m^2) and (b) its regional mean heating vertical profile (unit: K/day) with the domain ($24.5^\circ N$ – $30.1^\circ N$, $95.6^\circ E$ – $101.25^\circ E$). The purple line is the 2000 m elevation contour.

2.2. Analysis Methods

To diagnose the horizontal wave activity and eddy momentum and heat flux along the latitude–pressure cross-section in response to topographic forcing, zonal and meridional components of wave activity fluxes from Plumb [27] were used to obtain the spatial pattern of horizontal quasi-steady wave propagation. They can be expressed as follows:

$$F_s = \frac{p}{p_0} * \cos\varphi \left\{ \begin{array}{l} v'^2 - \frac{1}{2\Omega a \sin 2\varphi} \frac{\partial(v'\phi')}{\partial\lambda} \\ -u'v' + \frac{1}{2\Omega a \sin 2\varphi} \frac{\partial(u'\phi')}{\partial\lambda} \end{array} \right. \quad (1)$$

According to the relationship between the mean zonal wind acceleration and planetary wave activities [28], the eddy momentum and heat fluxes and their convergences are the main factors in the changing of upper tropospheric zonal wind. In this study, the zonal or regional mean of eddy momentum flux F_m and heat flux F_h were calculated as follows:

$$F_m = [u'v'] \quad (2)$$

$$F_h = [v'T'] \quad (3)$$

In (1)–(3), u , v , T , and ϕ signify zonal and meridional wind, temperature, and geopotential height. λ , φ , and Ω indicate longitude, latitude, and the Earth’s rotation rate. p is the pressure level and $p_0 = 1000$ hPa. The prime represents the zonal deviation of atmospheric variables and the square brackets ($[\cdot]$) indicate the zonal mean or regional mean operator.

3. Results

3.1. Simulated Zonal-Mean Circulation

Figure 3 shows the geopotential height, zonal wind, eddy temperature variance, and momentum and heat flux in the Notopo test. The geopotential height and zonal wind at 250 hPa and 500 hPa show the equivalent barotropic zonal mean patterns. The jet stream at the upper and mid-tropospheric levels are both located around 40° N. Meanwhile, the location of the intensive meridional gradient of geopotential height matches well with the maximum center of zonal wind, due to thermal wind balance (Figure 3a,b). The latitude–pressure cross-section of the jet stream is symmetric to the Equator, and it is generated with a maximum value of 30~35 m/s at 300 hPa around 40~45° N in the North hemisphere (Figure 3c). This indicates that the zonal symmetric radiative forcing can generally produce a zonal mean circulation. Due to strong internal variability and non-linearity in mid-latitude atmospheric circulation, the spatial patterns of eddy temperature variance, momentum, and heat flux should also be analyzed. The eddy temperature variance shows two peaks at mid-latitude: one with a stronger intensity of 3.0~3.6 K² in the lower troposphere, and another with weaker intensity around the tropopause (Figure 3d). The positive eddy momentum and heat flux mean that the momentum and heat are transported northward, and vice versa. According to the principle of zonal wind acceleration [27], the meridional gradient of eddy momentum flux ($\frac{\partial[u'v']}{\partial y}$) and the pressure-level gradient of eddy heat flux ($\frac{\partial[v'T']}{\partial p}$) are in proportion to the zonal wind tendency ($\frac{\partial u}{\partial t}$). In Figure 3e, the maximum (minimum) center of the eddy momentum flux is located around 20°~30° N (20°~30° S) in the upper tropospheric levels and reduces (intensifies) rapidly toward the center of the jet stream. For eddy heat flux, the maximum (minimum) center is consistent with the maximum center of eddy temperature variance in the North Hemisphere (South Hemisphere) (Figure 3d,f), and it reduces along pressure level (Figure 3f). The above results suggest that eddy momentum and heat flux play important roles in the maintenance of zonal mean circulation.

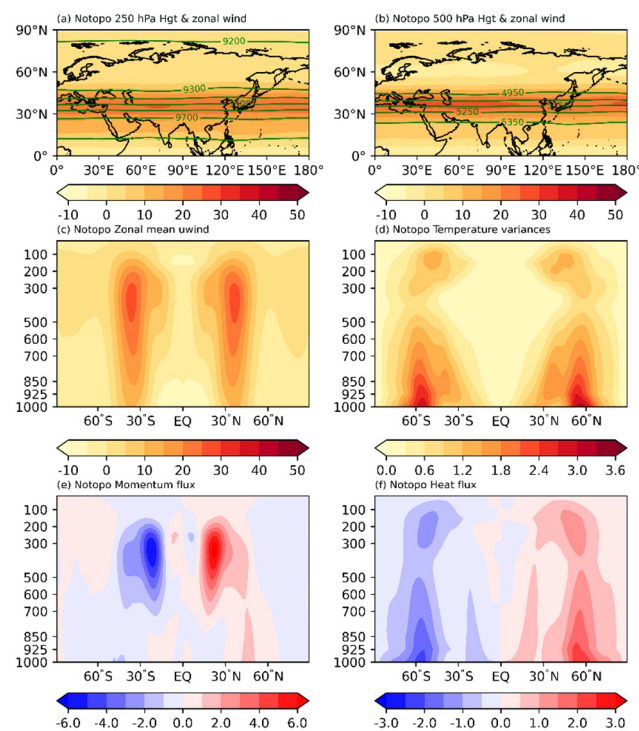


Figure 3. The climatological mean (a) 250 hPa geopotential height (green contour, intervals: 100 gpm, unit: gpm) and zonal wind (shaded, unit: m/s). (b) As in (a), but at 500 hPa. Pressure–latitude cross-section of (c) the zonal wind (unit: m/s), (d) meridional variances of temperature (unit: K²), (e) eddy momentum flux (unit: (m/s)²) and (f) heat flux (unit: m·k/s) in the Notopo test.

3.2. Topographic Effects on the Atmospheric Circulation and Planetary Wave Propagation

In the North Hemisphere, highlands, such as the Tibetan Plateau, Iranian Plateau, Mongolia Plateau, and the Rocky Mountains are located throughout the Eurasian continent and North American continent. To explore realistic and TP-dependent topographic effects on early spring atmospheric circulation, we defined the differences in simulated early spring climatology between Experiment Topo (TP_topo) and Notopo as the atmospheric response to realistic (TP-dependent) topographic forcing.

To display the spatial patterns of atmospheric circulation and the changes induced by realistic and TP-dependent topographic forcing, the zonal deviation of geopotential height and winds at 250 hPa and their differences are shown in Figure 4. First, the upper-tropospheric circulation in the Topo experiment shows a quasi-steady wave pattern over the Eurasian continent (Figure 4a), in which anticyclones are located over Central Asia and Northwest Pacific, cyclones extend from the southern Tibetan Plateau to Northeastern China, and the TP_topo experiment generally shows a similar circulation pattern as the Topo experiment. The strength of anticyclonic circulation over Central Asia in the TP_topo experiment is obviously stronger than that in the Topo experiment (Figure 4b). These results suggest that the topographic forcing over the TP may be the main dynamical effect on the formation of early spring atmospheric circulation. To further understand the realistic and TP-dependent topographic effects, the difference of zonal deviation geopotential height and plumb flux between the Topo (TP_topo) and Notopo experiments at 250 hPa are displayed (Figure 4c,d). The two results both show a similar pattern, which the anticyclone over Central Asia split into two branches of wave propagation; one propagates eastward and generates an anticyclone over the Northwest Pacific region, and the other propagates southeastward and generates a cyclone over the southern Iranian and Tibetan Plateau. Furthermore, the spatial patterns of zonal deviation geopotential height differences from these two tests are similar to the zonal deviation geopotential height result in the Topo experiment; therefore, this facilitates understanding on the importance of TP topographic forcing on the formation of atmospheric circulation over the Eurasian continent.

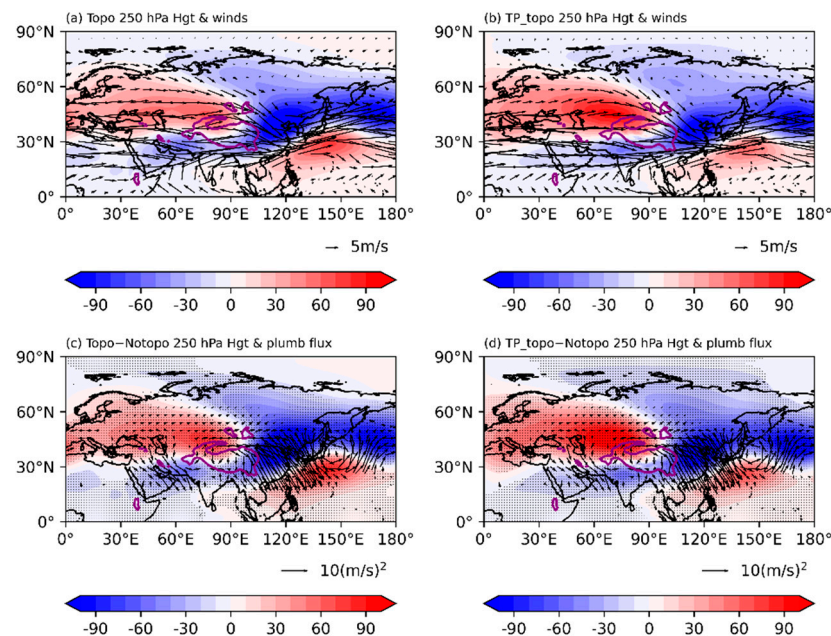


Figure 4. The climatological mean 250 hPa zonal deviation of geopotential height (shaded unit: gpm) and winds (vector, unit: m/s) in the (a) Topo and (b) TP_topo tests, and the differences in zonal deviation of 250 hPa geopotential height (shaded unit: gpm) and its associated wave flux (vector: $(\text{m/s})^2$) between the Topo and Notopo tests (c), and between the TP_topo and Notopo tests (d). Dots denote values and black vectors (c,d) exceeding the 95% confidence level of Student's *t* test. The purple line is the 2000 m elevation contour.

The changes in the upper tropospheric zonal wind and mid-lower tropospheric atmospheric circulation due to topographic forcing are shown in Figure 5. First, the changes of upper tropospheric zonal wind due to realistic and TP-dependent topographic forcing generally show the similar pattern, which an accelerated zonal wind extends from the south flank of the Iranian and Tibetan Plateaus to Japan, and a decelerated westerly appears in mid-latitude and the Northwestern Pacific region (Figure 5a,b). The similar patterns of the changes of zonal deviation geopotential height at 500 hPa (Figure 5c,d) and those at 250 hPa (Figure 4c,d) indicate that the atmospheric responses to topographic forcing show an equivalent barotropic structure. Furthermore, an accelerated westerly also appears in the subtropical region and Eastern Asian (Figure 5c,d), suggesting that TP-dependent topographic forcing may play an important role in the formation of the early spring subtropical and East Asian jet streams. To facilitate understanding of subtropical jet stream formation, latitude–pressure cross-sections of the regional mean (60.46° E–90° E) eddy momentum and heat flux differences between the TP_topo and Notopo experiments were calculated (Figure 5e,f). The eddy momentum flux in the upper tropospheric levels intensifies around 10°~40° N, while, it decreases over the tropical region and high-latitude region due to TP topographic forcing. Consequently, eddy momentum flux convergence ($\frac{\partial[u'v']}{\partial y} < 0$) (divergence ($\frac{\partial[u'v']}{\partial y} > 0$) appears on the south flank of plateaus and mid-latitude region (Iranian and Tibetan Plateaus) (Figure 5e). It results in zonal wind acceleration (deceleration) over these regions (Figure 5b). An intensified (decreased) eddy heat flux appears on the southern (northern) Iranian and Tibetan Plateaus. Its vertical convergence ($\frac{\partial[v'T']}{\partial p} < 0$) appears around 20°~30° N, which also can intensify the zonal wind over the subtropical region.

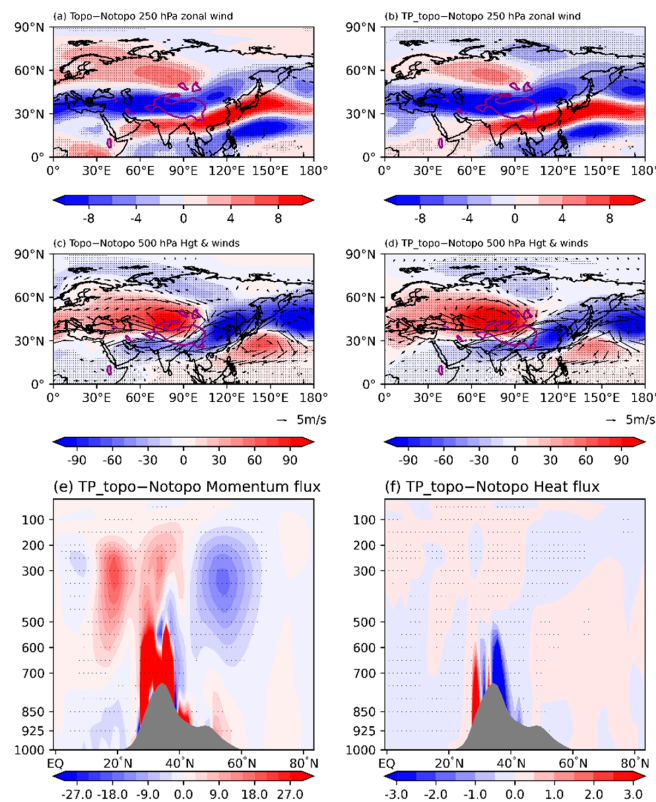


Figure 5. The differences in 250 hPa zonal wind (unit: m/s); zonal deviation of 500 hPa geopotential height (shaded unit: gpm) and winds (vector, unit: m/s); and pressure–latitude cross-section of eddy momentum flux (unit: (m/s)²) and eddy heat flux (unit: m·k/s) averaged from 60.46° E–90° E between the Topo and Notopo tests (a,c,e), and Tp_topo and Notopo tests (b,d,f). Dots denote values and black vectors exceeding the 95% confidence level of Student’s *t* test. The purple line is the 2000 m elevation contour.

3.3. Thermal Effects on the Atmospheric Circulation

To understand the mechanism of early spring sensible heating over the southeastern TP on the atmospheric circulation, the differences in the lower and upper tropospheric circulation, temperature, and vertical velocity between the TP_sh and the Topo tests were analyzed. According to the theory of thermal adaptation and Sverdrup balance, vertical diffusion heating can generate cyclonic (anticyclonic) circulation at lower (upper) tropospheric levels [4,29]. Thus, a significant anticyclonic circulation response extends from north of the—BOB to eastern TP at 250 hPa (Figure 6a); meanwhile, significant cyclonic circulation and an ascending motion response appears over the southeastern TP at the 27th hybrid level (approximately equivalent to 600~500 hPa over the TP) (Figure 6b,c). Regarding the surface temperature difference, a warm response at the 27th hybrid level due to vertical diffusion heating and horizontal temperature advection appears on the southeastern Tibetan Plateau (Figure 6d).

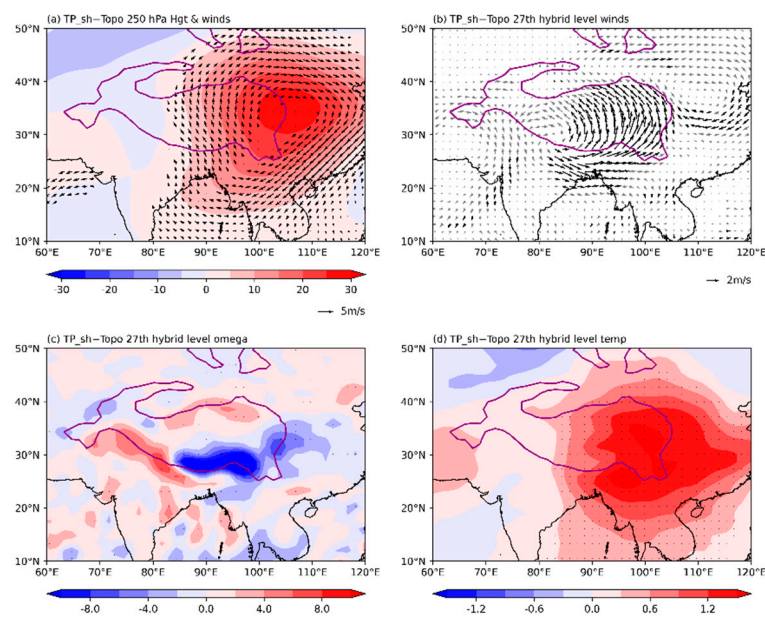


Figure 6. The differences in (a) zonal deviation of the 250 hPa geopotential height (shaded, unit: gpm) and winds (vector, unit: m/s), (b) 27th hybrid level winds (vector, unit: m/s), (c) 27th hybrid level temperature (shaded, unit: K), and (d) 27th hybrid level vertical velocity (shaded, unit: 0.01 Pa/s) between the TP_sh and Topo tests. Dots denote values and black vectors exceeding the 95% confidence level of Student's *t* test. The purple line is the 2000 m elevation contour.

To further understand the mechanism of the effect of early spring sensible heating on the regional static stability and vertical velocity responses that favor the appearance of precipitation, differences in the hybrid level-latitude and hybrid level-longitude cross-sections of potential temperature and vertical velocity between the TP_sh and Topo tests are shown in Figure 7. For the hybrid level-longitude cross-section, due to the pattern of vertical diffusion heating (Figure 2b), the intensity of potential temperature response decreases with height, exhibiting a statically unstable feature (Figure 7a). Meanwhile, there is an obviously ascending motion response appearing from 90° E–100° E (Figure 7b). While, an intensified response for static stability and descending motion appears from 70° E–90° E (Figure 7a,b). The hybrid level-latitude cross-section of potential temperature exhibits a warm response in the mid-lower tropospheric level over the TP and strong statically unstable pattern appears around 25° N (Figure 7c). Meanwhile, an obviously ascending motion response appears from 25° N–30° N, extending to mid-tropospheric level (Figure 7d). Taken together, statically unstable and ascending motion response over the Southeastern TP will help to the appearance of precipitation over this region.

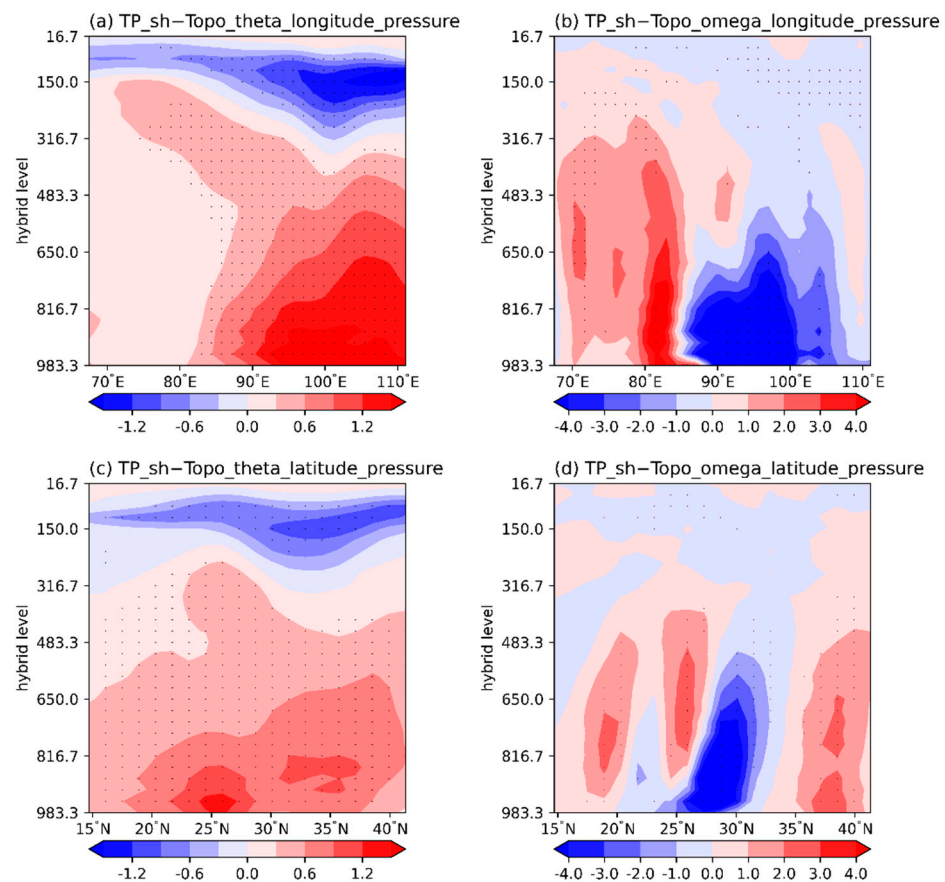


Figure 7. The differences in hybrid level–longitude averaged from 24.5° N– 30.1° N (a,b) and hybrid level–latitude averaged from 80.2° E– 98.4° E (c,d) cross-sections of potential temperature ((a,c), unit: K) and vertical velocity ((b,d), unit: 0.01 Pa/s) between the TP_sh and Topo tests. Dots denote values exceeding the 95% confidence level of Student’s *t* test.

To verify the circulation response to early spring sensible heating over the southeastern TP, the geopotential height, winds, and vertical velocity from the TP_sh test and climatological mean of those derived from ERA5 are shown in Figure 8. First, cyclonic shear and southwesterly winds over the southeastern TP are both shown in the TP_sh result and ERA5 reanalysis data. While, over the northern TP, the simulated northerly winds are obviously stronger than those in ERA5, and the geopotential height in the TP_sh test is less than that in ERA5 (Figure 8a,b). These biases may come from the absence of diabatic heating over the tropical regions. The spatial pattern of the lower tropospheric level vertical velocity in the TP_sh test generally matches with that in ERA5, especially in the southern TP and the western TP, where ascending motion appears (Figure 8c,d).

Climatological mean precipitation in March and February over the TP and its surrounding areas are also shown in Figure 9. The March precipitation over the southeastern TP is obviously stronger than that over other regions of the TP (Figure 9a), and there is little precipitation over the TP in February (Figure 9b). Climatological mean precipitation over the southeastern TP increases by nearly 20 mm from February to March (Figure 9c). Combining simulated southerly winds at 500 hPa (Figure 8a) and ascending motion at the 27th hybrid level (Figure 8c) from TP_sh test, it is further revealed that sensible heating over the southeastern TP can be an important thermal forcing on the early spring precipitation over abovementioned region.

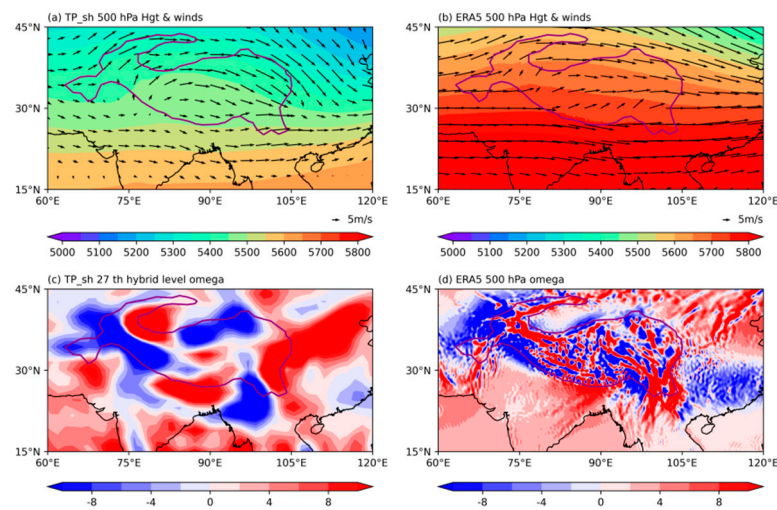


Figure 8. The simulated 500 hPa geopotential height (shaded, unit: gpm) and winds (vector, unit: m/s) in the TP_sh experiment (a), (b) as in (a), but with the climatology results derived from ERA5. The simulated vertical velocity (shaded, unit: 0.01 Pa/s) at the 27th hybrid level in the TP_sh experiment (c), (d) as in (c), but with the climatology result at 500 hPa derived from ERA5. The purple line is the 2000 m elevation contour.

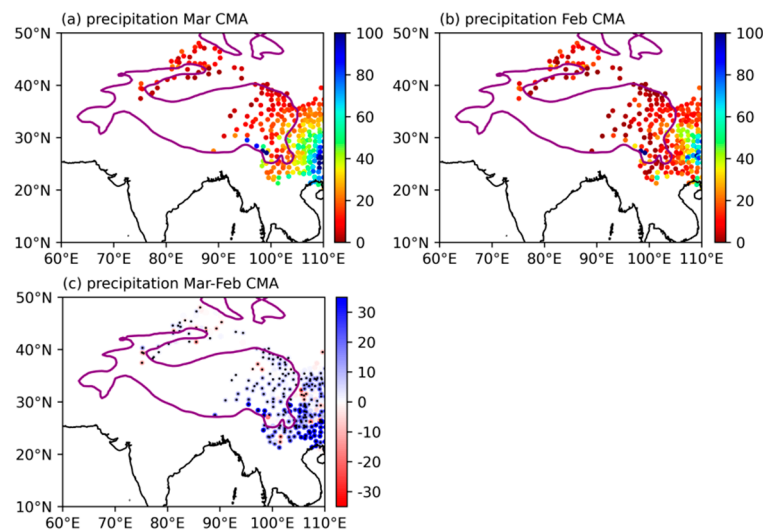


Figure 9. The climatological mean of accumulated precipitation (unit: mm) derived from the China Meteorological Administration in March (a) and February (b), and their differences (c). Dots denote values exceeding the 95% confidence level of Student's *t* test. The purple line is the 2000 m elevation contour.

4. Conclusions and Discussion

The effect of topographical and thermal forcing on the formation of favorable early spring atmospheric circulation, vertical velocity and static stability patterns to early spring precipitation over the southeastern Tibetan Plateau were investigated by using a set of realistic and Tibetan Plateau-dependent topographic forcing, as well as sensible heating numerical experiments. The results indicate that Tibetan Plateau-dependent topographic forcing may be the main dynamical effect on the formation of early spring atmospheric circulation through triggering an equivalent barotropic quasi-steady Rossby wave that propagates southeastward to the southeastern Tibetan Plateau, generating low pressure and cyclonic circulation. The eddy momentum and heat fluxes changes can maintain the subtropical jet stream in the south flank of the Iranian and Tibetan Plateaus through interaction between the planetary wave activity and zonal wind. Moreover, the early spring

sensible heating over the southeastern Tibetan Plateau can trigger cyclonic and anticyclonic circulations at lower and upper tropospheric levels based on thermal adaptation. It also causes ascending motion and statically instable over the southeastern Tibetan Plateau, which will further favor precipitation over this region. The validation of the circulation pattern at 500 hPa between the TP_sh test and ERA5 reanalysis data, and analysis of the precipitation in the southeastern Tibetan Plateau further reveals that sensible heating is an important thermal factor in generation of early spring precipitation over the southeastern Tibetan Plateau.

In the present study, we only explored the effect of topographic and thermal forcing over the Tibetan Plateau on the formation of favorable atmospheric circulation to precipitation over the southeastern Tibetan Plateau. However, tropical sea surface temperature and diabatic heating may also be important factors in its generation. Moreover, the relationship between land–air interaction and spring precipitation over the Tibetan Plateau is still unclear. In future study, the mechanism of the seasonal evolution of spring precipitation over the Tibetan Plateau and its relation with soil temperature and moisture, sensible heating, and vegetation will be further explored within the framework of land–air coupled numerical experiments.

Author Contributions: Conceptualization, all authors, data curation, Y.Y.; Formal analysis, Y.Y.; Funding acquisition, Z.H., M.L., H.Y. and W.M.; Writing-original draft, Y.Y.; Writing-reviewing and editing, Z.H., M.L., H.Y., W.M. and W.F. All authors have read and agreed to the published version of the manuscript.

Funding: This research was funded by the Second Tibetan Plateau Scientific Expedition and Research Program (2019QZKK0103), the National Natural Science Foundation of China (91837208, 41830650, 41675106, 42075043, 42122034), the Strategic Priority Research Program of the Chinese Academy of Sciences (Grant No. XDA2006010101), the Systematic Major Project of the China Railway (Grant No. P2021G047), the Youth Innovation Promotion Association CAS, and Science and technology project of Gansu Province (21JR7RA067).

Institutional Review Board Statement: Not applicable.

Informed Consent Statement: Not applicable.

Data Availability Statement: The JRA-55 data. Available online: <https://rda.ucar.edu> (accessed on 17 June 2021). The ERA5 data. Available online: <https://cds.climate.copernicus.eu> (accessed on 20 October 2020). The precipitation data provided by the China Meteorological Administration. Available online: <http://www.nmic.cn> (accessed on 12 May 2018).

Acknowledgments: We would like to express our thanks for the availability of GCM from the website <https://www.cesm.ucar.edu/models> (accessed on 28 May 2022). We also thank three anonymous reviewers for their constructive and helpful comments and suggestions, which were very helpful to improve our papers.

Conflicts of Interest: The authors declare no conflict of interest.

References

1. Xu, X.; Lu, C.; Shi, X.; Gao, S. World water tower: An atmospheric perspective. *Geophys. Res. Lett.* **2008**, *35*, L20815. [CrossRef]
2. He, Y.; Tian, W.; Huang, J.; Wang, G.; Ren, Y.; Yan, H.; Yu, H.; Guan, X.; Hu, H. The mechanism of increasing summer water vapor over the Tibetan Plateau. *J. Geophys. Res. Atmos.* **2021**, *126*, e2020JD034166. [CrossRef]
3. Liu, L.; Ma, Y.; Yao, N.; Ma, W. Diagnostic analysis of a regional heavy snowfall event over the Tibetan Plateau using NCEP reanalysis data and WRF. *Clim. Dyn.* **2008**, *56*, 2451–2467. [CrossRef]
4. Wu, G.; Liu, Y.; Zhang, Q.; Duan, A.; Wang, T.; Wan, R.; Liu, X.; Li, W.; Wang, Z.; Liang, X. The influence of mechanical and thermal forcing by the Tibetan Plateau on Asian climate. *J. Hydrometeorol.* **2007**, *8*, 770–789. [CrossRef]
5. Wu, G.; Liu, Y.; He, B.; Bao, Q.; Duan, A.; Jin, F-F. Thermal controls on the Asian summer monsoon. *Sci. Rep.* **2012**, *2*, 404. [CrossRef]
6. Zhao, Y.; Duan, A.; Wu, G. Interannual variability of late-spring circulation and diabatic heating over the Tibetan Plateau associated with Indian Ocean forcing. *Adv. Atmos. Sci.* **2018**, *35*, 927–941. [CrossRef]
7. Kuang, X.; Zhang, Y. Seasonal Variation of the East Asian subtropical Westerly Jet and Its association with heating fields over East Asia. *Adv. Atmos. Sci.* **2005**, *22*, 831–840.

8. Liu, X.; Liu, Y.; Wang, X.; Wu, G. Large-scale dynamics and moisture sources of the precipitation over the western Tibetan Plateau in boreal winter. *J. Geophys. Res. Atmos.* **2020**, *125*, e2019JD032133. [[CrossRef](#)]
9. Yang, K.; Wu, H.; Qin, J.; Lin, C.; Tang, W.; Chen, Y. Recent climate changes over the Tibetan Plateau and their impacts on energy and water cycle: A review. *Glob. Planet. Change* **2014**, *112*, 79–91. [[CrossRef](#)]
10. Ouyang, L.; Yang, K.; Lu, H.; Chen, Y.; La, Z.; Zhou, X.; Wang, Y. Ground based observations reveal unique valley precipitation patterns in the central Himalaya. *J. Geophys. Res. Atmos.* **2020**, *125*, e2019JD031502. [[CrossRef](#)]
11. Xiao, Z.; Duan, A. Impacts of Tibetan Plateau snow cover on the interannual variability of the East Asian summer monsoon. *J. Clim.* **2016**, *29*, 8495–8514. [[CrossRef](#)]
12. Duan, A.; Xiao, Z.; Wang, Z. Impacts of the Tibetan Plateau winter/spring snow depth and surface heat source on Asian summer monsoon: A review. *Chin. J. Atmos. Sci.* **2018**, *42*, 755–766. (In Chinese)
13. Han, Y.; Ma, W.; Yang, Y.; Ma, Y.; Xie, Z.; Sun, G.; Menenti, M.; Su, B. Impacts of the Silk Road pattern on the interdecadal variations of the atmospheric heat source over the Tibetan Plateau. *Atmos. Res.* **2021**, *260*, 105696. [[CrossRef](#)]
14. Bolin, B. On the influence of the earth's orography on the general character of the westerlies. *Tellus* **1950**, *2*, 184–195. [[CrossRef](#)]
15. Yeh, T. The circulation of the high troposphere over China in the winter of 1945–1946. *Tellus* **1950**, *2*, 173–183. [[CrossRef](#)]
16. Zhou, X.; Gu, Z. The influence of the slope of a plateau on the movement of troughs and ridges. *Acta Meteorol. Sin.* **1958**, *29*, 99–103. (In Chinese)
17. Duan, A.; Liu, S.; Zhao, Y.; Gao, K.; Hu, W. Atmospheric heat source/sink dataset over the Tibetan Plateau based on satellite and routine meteorological observations. *Big Earth Data* **2018**, *2*, 179–189. [[CrossRef](#)]
18. Wan, R.; Wu, G. Mechanism of the Spring Persistent Rains over southeastern China. *Sci. China Earth Sci.* **2007**, *50*, 130–144. [[CrossRef](#)]
19. Ren, R.; Xia, X.; Rao, J. Topographic forcing from East Asia and North America in the northern winter stratosphere and their mutual interference. *J. Clim.* **2019**, *32*, 8639–8658. [[CrossRef](#)]
20. Held, I.; Suarez, M. A proposal for the intercomparison of the dynamical cores of atmospheric general circulation models. *Bull. Am. Meteorol. Soc.* **1994**, *75*, 1825–1830. [[CrossRef](#)]
21. Schneider, T.; Bordoni, S. Eddy-mediated regime transitions in the seasonal cycle of a Hadley circulation and implications for monsoon dynamics. *J. Atmos. Sci.* **2008**, *65*, 915–934. [[CrossRef](#)]
22. Siu, L.; Bowman, K. Forcing of the upper-tropospheric monsoon anticyclones. *J. Atmos. Sci.* **2019**, *76*, 1937–1954. [[CrossRef](#)]
23. Schneider, T. The tropopause and the thermal stratification in the extratropics of a dry atmosphere. *J. Atmos. Sci.* **2004**, *61*, 1317–1340. [[CrossRef](#)]
24. Kobayashi, S.; Ota, Y.; Harada, Y.; Ebata, A.; Moriya, M.; Onoda, H.; Onogi, K.; Kamahori, H.; Kobayashi, C.; Endo, H.; et al. The JRA-55 Reanalysis: General Specifications and Basic Characteristics. *J. Meteorol. Soc. Jpn.* **2015**, *93*, 5–48. [[CrossRef](#)]
25. Sardeshmukh, P.; Hoskins, B. Spatial Smoothing on the Sphere. *Mon. Weather Rev.* **1984**, *112*, 2524–2529. [[CrossRef](#)]
26. Hersbach, H.; Bell, B.; Berrisford, P.; Hirahara, S.; Horányi, A.; Muñoz-Sabater, J.; Nicolas, J.; Peubey, C.; Radu, R.; Schepers, D.; et al. The ERA5 global reanalysis. *Q. J. R. Meteorol. Soc.* **2020**, *146*, 1999–2049. [[CrossRef](#)]
27. Plumb, R. On the three-dimensional propagation of stationary waves. *J. Atmos. Sci.* **1985**, *42*, 217–229. [[CrossRef](#)]
28. Andrews, D.; McIntyre, M. Planetary Waves in Horizontal and Vertical Shear: The Generalized Eliassen-Palm Relation and the Mean Zonal Acceleration. *J. Atmos. Sci.* **1976**, *33*, 2031–2048. [[CrossRef](#)]
29. Wu, G.; Liu, Y. Thermal adaptation, overshooting, dispersion, and subtropical high. Part I: Thermal adaptation and overshooting. *Chin. J. Atmos. Sci.* **2000**, *24*, 433–446. (In Chinese)